causes the lattice to lose its distortion, and a strong coupling between the hole and the lattice results. Extrapolating this picture, we expect the diminishing of the spin-Peierls distortion above the pseudogap temperature T^* (note that $T^* = T_c$ for optimally doped Bi2212). As a result, the coupling between the photo-hole and the lattice is weakened. The observation of significant isotope dependences of T^* (refs 27), J and various low-temperature spin properties[28,29] supports this scenario. We believe that the above cooperative interplay between electron pairing and electron–lattice interaction outlines the role that phonons play in high-temperature superconductivity. The above proposal has been shown theoretically to work in one dimension[30] and in a two-leg Hubbard ladder incorporating the electron–phonon interaction (A. Seidel, H. H. Lin and D.-H.L., manuscript in preparation). □

1. Franck, J. P. in *Physical Properties of High Temperature Superconductors IV* (ed. Ginsberg, D. M.) 189–293 (World Scientific, Singapore, 1994).
2. Pytte, E. Peierls instability in Heisenberg chains. *Phys. Rev. B* **10**, 4637–4642 (1974).
3. Müller, K. A. On the oxygen isotope effect and apex anharmonicity in high-T_c cuprates. *Z. Phys. B* **80**, 193–201 (1990).
4. Bianconi, A. *et al.* Determination of the local lattice distortions in the CuO_2 plane of $La_{1.85}Sr_{0.15}CuO_4$. *Phys. Rev. Lett.* **76**, 3412–3415 (1996).
5. Gweon, G.-H., Zhou, S. Y. & Lanzara, A. Strong influence of phonons on the electron dynamics of $Bi_2Sr_2CaCu_2O_{8+\delta}$. *J. Phys. Chem. Solids* (in the press).
6. Lanzara, A. *et al.* Evidence for ubiquitous strong electron-phonon coupling in high-temperature superconductors. *Nature* **412**, 510–514 (2001).
7. Allen, J. W., Gweon, G.-H., Claessen, R. & Matho, K. Fermi liquids and non-Fermi liquids—The view from photoemission. *J. Phys. Chem. Solids* **56**, 1849–1853 (1995).
8. Bogdanov, P. V. *et al.* Evidence for an energy scale for quasiparticle dispersion in $Bi_2Sr_2CaCu_2O_8$. *Phys. Rev. Lett.* **85**, 2581–2584 (2000).
9. Kaminski, A. *et al.* Renormalization of spectral lineshape and dispersion below T_c in $Bi_2Sr_2CaCu_2O_{8+\delta}$. *Phys. Rev. Lett.* **86**, 1070–1073 (2001).
10. Johnson, P. D. *et al.* Doping and temperature dependence of the mass enhancement observed in the cuprate $Bi_2Sr_2CaCu_2O_{8+\delta}$. *Phys. Rev. Lett.* **87**, 177007–177010 (2001).
11. Zhou, X. J. *et al.* Universal nodal Fermi velocity. *Nature* **423**, 398 (2003).
12. Sato, T. *et al.* Observation of band renormalization effects in hole-doped high-T_c superconductors. *Phys. Rev. Lett.* **91**, 157003 (2003).
13. Eliashberg, G. M. Interactions between electrons and lattice vibrations in a superconductor. *Zh. Eksp. Teor. Fiz.* **38**, 966–976 (1960); *Sov. Phys. JETP* **11**, 696–702 (1960).
14. Verga, S., Knigavko, A. & Marsiglio, F. Inversion of angle-resolved photoemission measurements in high-T_c cuprates. *Phys. Rev. B* **67**, 054503 (2003).
15. Hwang, J., Timusk, T. & Gu, G. D. High-transition-temperature superconductivity in the absence of the magnetic-resonance mode. *Nature* **427**, 714–717 (2004).
16. Rotenberg, E., Schaefer, J. & Kevan, S. D. Coupling between adsorbate vibrations and an electronic surface state. *Phys. Rev. Lett.* **84**, 2925–2928 (2000).
17. Cuk, T. *et al.* Coupling of the B_{1g} phonon to the anti-nodal electronic states of $Bi_2Sr_2Ca_{0.92}Y_{0.08}Cu_2O_{8+\delta}$. Preprint condmat/0403521 at ⟨http://xxx.lanl.gov⟩ (2004); *Phys. Rev. Lett.* (submitted).
18. Zhao, G. M., Hunt, M. B., Keller, H. & Müller, K. A. Evidence for polaronic supercarriers in the copper oxide superconductors $La_{2-x}Sr_xCuO_4$. *Nature* **385**, 236–240 (1997).
19. Crespi, V. H. & Cohen, M. L. Anharmonic phonons and the anomalous isotope effect in $La_{2-x}Sr_xCuO_4$. *Phys. Rev. B* **44**, 4712–4715 (1991).
20. Sawatzky, G. A. Testing Fermi liquid models. *Nature* **342**, 480–481 (1989).
21. Shen, Z.-X. & Schrieffer, J. R. Momentum, temperature, and doping dependence of photoemission lineshape and implications for the nature of the pairing potential in high-T_c superconducting materials. *Phys. Rev. Lett.* **78**, 1771–1774 (1997).
22. Norman, M. R. *et al.* Unusual dispersion and line shape of the superconducting state spectra of $Bi_2Sr_2CaCu_2O_8$. *Phys. Rev. Lett.* **79**, 3506–3509 (1997).
23. Paci P. *et al.* Polaronic and nonadiabatic phase diagram from anomalous isotope effects. Preprint condmat/0405053 at ⟨http://xxx.lanl.gov⟩ (2004).
24. Pan, S. H. *et al.* Microscopic electronic inhomogeneity in the high-T_c superconductor $Bi_2Sr_2CaCu_2O_{8+\delta}$. *Nature* **413**, 282–285 (2001).
25. Anderson, P. W. Theory of dirty superconductors. *J. Phys. Chem. Solids* **11**, 26–30 (1959).
26. Crawford, M. K. *et al.* Oxygen isotope effect and structural phase transitions in La_2CuO_4-based superconductors. *Science* **250**, 1390–1394 (1990).
27. Lanzara, A. *et al.* Oxygen-isotope shift of the charge-stripe ordering temperature in $La_{2-x}Sr_xCuO_4$ from X-ray absorption spectroscopy. *J. Phys. Condens. Matter* **11**, L541–L546 (1999).
28. Shengelaya, A., Brunn, M., Kochelaev, B. I., Safina, A., Conder, K. M. & Müller, K. A. A metallic phase in lightly doped $La_{2-x}Sr_xCuO_4$ observed by electron paramagnetic resonance. Preprint cond-mat/0310152 at ⟨http://xxx.lanl.gov⟩ (2003); *Phys. Rev. Lett.* (in the press).
29. Zech, D., Keller, H., Conder, K., Kaldis, E., Liarokapis, E., Poulakis, N. & Müller, K. A. Site-selective oxygen isotope effect in optimally doped $YBa_2Cu_3O_{6+x}$. *Nature* **371**, 681–683 (1994).
30. Zimanyi, G. T., Kivelson, S. A. & Luther, A. Superconductivity from predominantly repulsive interactions in quasi one-dimensional systems. *Phys. Rev. Lett.* **60**, 2089–2092 (1988).

....

Colloidal nanocrystal heterostructures with linear and branched topology

Delia J. Milliron[1,2], **Steven M. Hughes**[1,2], **Yi Cui**[1,2], **Liberato Manna**[1,2]*, **Jingbo Li**[3], **Lin-Wang Wang**[3] & **A. Paul Alivisatos**[1,2]

[1]*Department of Chemistry, University of California,* [2]*Materials Science Division, and* [3]*Computational Research Division, Lawrence Berkeley National Laboratory, Berkeley, California, 94720, USA*

* Present address: National Nanotechnology Lab of INFM, Via Arnesano, 73100 Lecce Lecce, Italy

....

The development of colloidal quantum dots has led to practical applications of quantum confinement, such as in solution-processed solar cells[1], lasers[2] and as biological labels[3]. Further scientific and technological advances should be achievable if these colloidal quantum systems could be electronically coupled in a general way. For example, this was the case when it became possible to couple solid-state embedded quantum dots into quantum dot molecules[4,5]. Similarly, the preparation of nanowires with linear alternating compositions—another form of coupled quantum dots—has led to the rapid development of single-nanowire light-emitting diodes[6] and single-electron transistors[7]. Current strategies to connect colloidal quantum dots use organic coupling agents[8,9], which suffer from limited control over coupling parameters and over the geometry and complexity of assemblies. Here we demonstrate a general approach for fabricating inorganically coupled colloidal quantum dots and rods, connected epitaxially at branched and linear junctions within single nanocrystals. We achieve control over branching and composition throughout the growth of nanocrystal heterostructures to independently tune the properties of each component and the nature of their interactions. Distinct dots and rods are coupled through potential barriers of tuneable height and width, and arranged in three-dimensional space at well-defined angles and distances. Such control allows investigation of potential applications ranging from quantum information processing to artificial photosynthesis.

Unlike vapour–liquid–solid (VLS)- or SLS-grown nanowires, anisotropic nanocrystals in homogeneous solutions grow without the benefit of catalyst activation of one end. Hence, heterostructure growth in colloidal nanocrystals has so far been limited to core–shell structures that serve primarily to further isolate quantum dots from their environment[10,11,12,13,14]. An elegant extension of core–shell growth enabled concentric alternating layers of CdS and HgS, which have a type I (nested) band alignment[15,16]. Control over the electronic structure of concentric heterostructures is, however, restricted by their simple geometry and by strain due to lattice mismatch, which typically limits the thickness of each layer to a few monolayers or less. Heterostructures based on nanorods permit

more complexity and their properties are fully tuneable because strain does not limit their dimensions.

Anisotropic colloidal heterostructures are fabricated by sequential growth of semiconductor dots and rods of different materials, with the potential for branched connectivity in each generation. Branching is introduced through crystal phase control[17,18,19], so the large class of semiconductors exhibiting zincblende–wurtzite polytypism[20] could be incorporated into branched heterostructures by these methods. Recently, limited phase control enabled the high-yield synthesis of tetrapod-shaped nanocrystals of a single material, CdTe[19], effectively arranging four quantum rods of the same composition around a central dot. This fundamental branched structure results from nucleation in the cubic zincblende phase with subsequent anisotropic growth in the hexagonal wurtzite phase. Here, we demonstrate that branched and linear junctions can be created not just at nucleation, but at any point during the growth of heterostructures. Considering two generations of growth within this paradigm, four basic structures can be postulated and were synthesized. The first-generation nanostructures can be linear, wurtzite rods, or branched tetrapods. On these two basic structures, a second material is grown in either branched or linear fashion (Figs 1 and 2). The dimensions of each generation define the degree of quantum confinement and are controlled by methods developed for nanorod growth[21]. The terminal rods and dots are coupled through the tuneable barrier defined by the first generation, whereas more generations of growth would produce structures incorporating even more complex interactions. In a preliminary exploration

of novel properties of nanocrystal heterostructures, long-range photoinduced charge separation has been achieved in type II (staggered band) heterostructures, as shown by the quenching of nanocrystal luminescence. Type I heterostructures permit tuneable exchange coupling between the terminal quantum dots or rods.

New methods were developed to grow a second material selectively on the ends of nanorods and to create branch points at will. Unlike core–shell nanocrystals, heterostructures were grown in the kinetic control regime previously exploited for CdSe nanocrystal shape control[17]. First-generation structures were grown by modifications of previously reported methods for preparing elongated nanocrystals[17,18,19,21]. In all cases, cadmium oxide complexed by alkylphosphonic acids was used as the cation precursor[18]. The anion precursor (elemental Se, S or Te dissolved in tri(n-alkylphosphine)) was injected at a temperature between 280 and 320 °C to initiate growth. Linear heterojunctions were formed when precursors for a second material were added to a growth solution containing preformed nanorods or tetrapods. Branched junctions were introduced preferentially at high supersaturation of these precursors. The second generation was typically grown without isolation of the nanocrystals by using an excess of cadmium in the first step and injecting the anion precursor for the second material. Thus, in this work, all the reported heterostructures have cadmium as a common cation. Linearly extended rods were synthesized with CdS rods and CdSe extensions, while the other structures were synthesized with CdSe in the first and CdTe in the second generation. Branched rods were also synthesized with CdS rods and CdTe branches. Similar
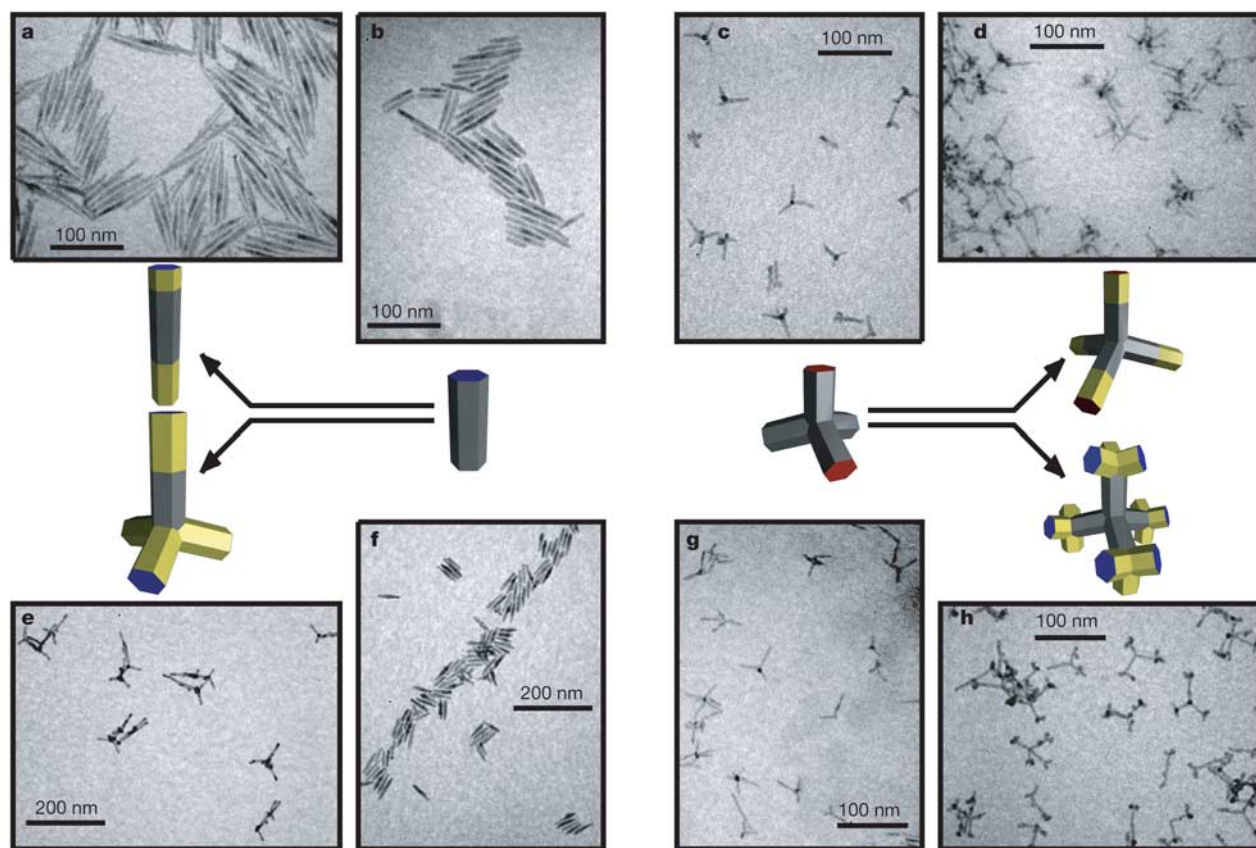

Figure 1 Survey of nanocrystal heterostructures. Extended rods (**a**) were formed first by growing CdS nanorods (**b**), then adding CdSe extensions to each end. Branched rods (**e**) result from nucleation of CdTe on either end of CdSe nanorods (**f**). A CdTe zincblende region at one end creates the branch point. CdSe tetrapods (**c**, **g**) comprise a zincblende core and four wurtzite arms. Extending each arm linearly with CdTe yields extended tetrapods (**d**). Branched tetrapods (**h**) result from nucleation of CdTe zincblende branch points on the end of each arm. The model sequences illustrate the growth processes. In each case, the first generation is shown in grey and the second in yellow, while red and blue indicate the unique crystal faces of the wurtzite structure.

results were achieved by isolation of the first-generation nanocrystals and reintroduction of cadmium precursor before injecting the second anion precursor, implying extensibility to heterostructures incorporating semiconductors that do not share common ions. This method may also produce more compositionally abrupt heterojunctions. All of the heterostructures could be readily dispersed in common organic solvents, such as toluene and chloroform, and were prepared with high yield without any post-synthetic separation.

Reversing the growth sequence under similar synthetic conditions changed the growth pattern of the second material from selective on the ends to more homogeneous core–shell growth. For example, growing CdTe followed by CdSe, we succeeded in synthesizing type II core–shell tetrapods (Supplementary Fig. 1). As observed previously for core–shell nanorods[22], elongated growth from the ends of core–shell tetrapods proceeds only after several monolayers of shell have formed and strain limits further homogeneous growth. In contrast, in branched and linear heterostructures, we suggest that the difference in surface energy between two materials favours end-selective growth. Although, in principle, they limit materials selection for a given topology, these observations suggest that any pair of materials in this class[20] could be combined in core–shell or in end-selective structures by reversing their growth order.

Several techniques were applied to establish the end selectivity of heteroepitaxy in these nanocrystal structures. Nanoprobe X-ray energy dispersive spectrometry (EDS) was used to examine the local atomic composition of the heterostructures[3]. The resulting EDS line scans (Fig. 3) confirm the presence of Te at either end of branched-rod heterostructures, Se in the central rod, and Cd throughout. The apparent remnant tellurium signal in the middle section is an artefact that results from partial overlap with an adjacent Cd peak and is observed in similar magnitude in CdSe nanorods containing no Te. Results on extended rods (Supplementary Fig. 2) similarly confirm end long growth of thinner CdSe extensions on CdS rods. While a sufficiently small spot size was used, the spatial resolution of the EDS data was limited by the drift of the instrument so that it remains uncertain how compositionally abrupt the interfaces are. The apparently few-nanometre width of

the composition gradient is an upper bound. To see more clearly whether the end long growth is accompanied by the formation of a thin shell, the powder X-ray diffraction patterns at different stages of growth were examined (Supplementary Fig. 3). Although noticeable peak shifts due to strain result from the growth of uniform

Figure 3 Analytical electron microscopy of heterojunctions. a, A nanoprobe EDS line scan (a) along a branched rod (inset) confirms CdTe growth on CdSe. The high-intensity spike corresponds to the CdTe arm projecting out of the plane from the branch point. b–d, Representative spectra from the CdTe portion (b) and CdSe portion (c) of the heterostructure, and shown together with a spectrum of a pure CdSe rod (d).
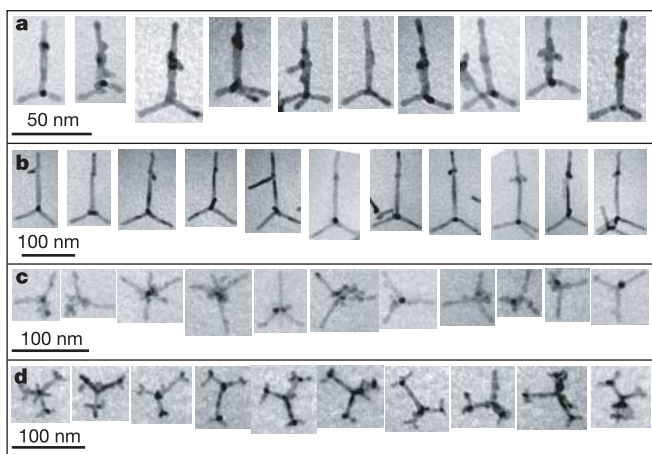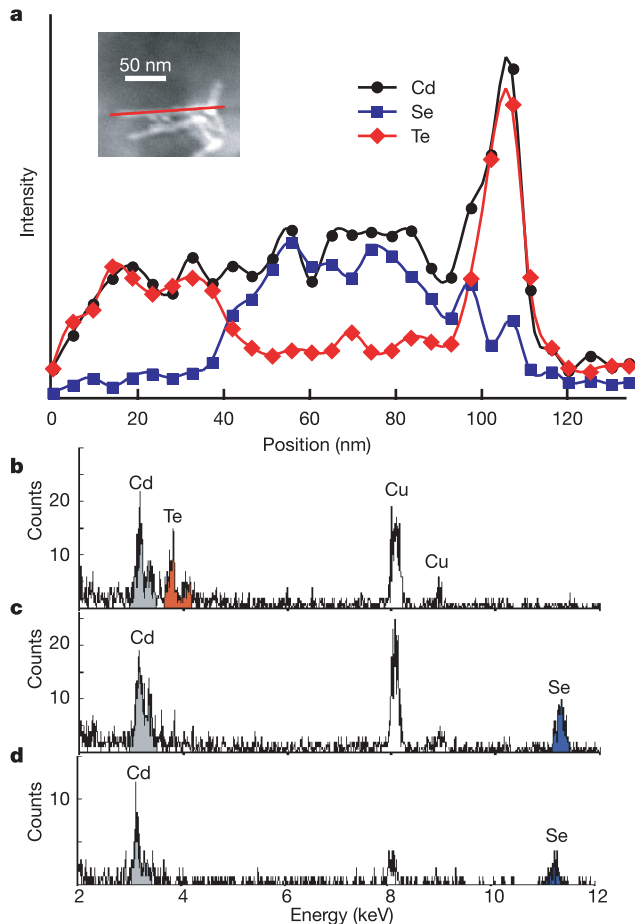

Figure 2 A closer look at nanocrystal heterostructures. Isolated particles allow examination of structural aspects such as 'back branching' in branched rods (a and b) and extended tetrapods (c) and structural isomers in branched tetrapods (d). Branches projecting from the linear junction at an angle back along the original rod arise from stacking faults at the heterojunction and are consistent with the symmetry relationships between the zincblende and wurtzite phases. Secondary branches in branched tetrapods (d) grow either staggered or eclipsed with respect to the arms of the original tetrapod. Heterostructures in a, c and d are CdTe grown on CdSe, and in b are CdTe grown on CdS.
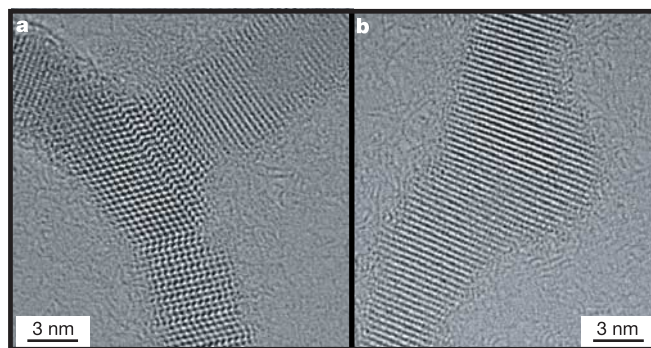

Figure 4 High-resolution electron microscopy of heterojunctions. a, HRTEM of a branch point shows a zincblende core and wurtzite branches of CdTe and an original wurtzite rod (upper right) of CdSe. b, Examination of a linear junction between CdSe (upper right) and CdTe reveals continuous wurtzite growth.

shells even one monolayer thick on nanorods[22,23], we observed no obvious peak shifts in the case where growth occurs on the ends only. Furthermore, statistical length and diameter distributions extracted from transmission electron microscope (TEM) images (Supplementary Fig. 4) indicate no significant change in diameter upon growth of the second material. For example, the radii of the arms of one batch of CdSe tetrapods were 2.9 ± 0.4 nm before growing CdTe extensions, and 2.9 ± 0.5 nm afterwards. CdS nanorod radii were 3.6 ± 0.4 nm before and 3.9 ± 0.5 nm after growing CdSe extensions where, owing to the tapered shapes of the CdS rods and of the heterostructures, the radius is taken as the maximum. The small increase in radius is consistent with the formation of at most one monolayer of CdSe on the sides of the CdS nanorods. Finally, although several of these heterostructures are type II, their optical absorption spectra lack distinctive sub-band gap tails like those observed for type II core–shell quantum dots[14] and for our core–shell tetrapods (Supplementary Fig. 5). Owing to the very small scale of these heterostructures, no technique allows us to eliminate the possibility that a very thin (one monolayer) shell grows by overgrowth or ion exchange; however, taken together, these results strongly indicate selective heteroepitaxial growth on the ends of nanorods and tetrapods.

The topology of each generation is determined by the initial growth phase of the nucleating material. Nanorods and tetrapod
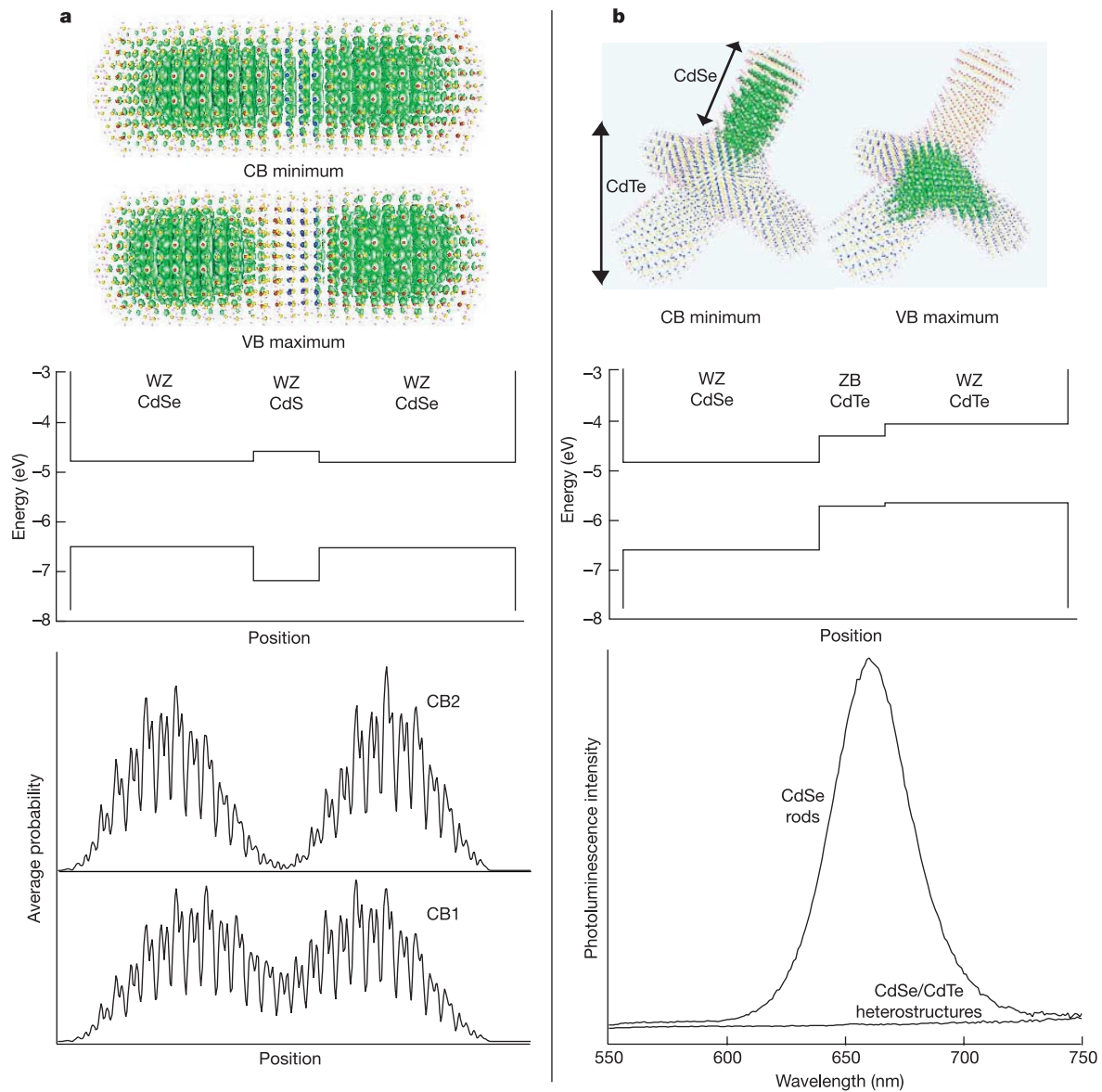

Figure 5 Optoelectronic properties of type I and type II heterostructures. **a**, *Ab initio* calculation of type I CdSe/CdS/CdSe heterostructures reveals electronic coupling. Isosurfaces of the lowest-energy electron and highest-energy hole states (top) show the even distribution of probability between the two terminal CdSe quantum rods. The band alignment illustrates the formation of coupled wells for electrons and holes. The cross section-averaged probability for the lowest-energy conduction band state (CB1) shows significant penetration of the CdS barrier, while the next conduction band state (CB2) has a longitudinal node. The diameter of the calculated rod is about 2 nm, the total length is about 9.5 nm, and there are in total 2,002 atoms. The thickness of the CdS is three monolayers. **b**, In type II CdSe/CdTe heterostructures the electron and hole are spatially separated. Their distribution agrees qualitatively with the expected band alignment. The photoluminescence of CdSe rods immediately before adding CdTe branches is easily observed (bottom), whereas in heterostructures, charge separation strongly quenches the luminescence. For the calculated tetrapod, each branch has a diameter of 2.2 nm and a length of 4.2 nm. There are in total 3,685 atoms in the tetrapod.

arms grow in the wurtzite structure, elongated along the unique *c* axis. Invariably, such nanocrystals contain a statistical distribution of stacking faults, which convert the growth to zincblende and back to wurtzite along the rod, sometimes leading to kinks or other irregularities[21]. High-resolution transmission electron microscopy (HRTEM) of linear junctions found in extended rods and tetrapods, and in branched rods, reveals a continuation of anisotropic wurtzite growth in the second semiconductor (Fig. 4 and Supplementary Fig. 6), often accompanied by a high concentration of stacking faults. At these junctions, the small diameter allows dislocation-free epitaxial growth despite fairly large lattice mismatches. The hetero-structures with the largest mismatch (CdS/CdTe) easily accommodated an 11% mismatch (Supplementary Fig. 6). In HRTEM, branch points could most easily be observed by imaging branched rods that were missing one of the three CdTe branches (Fig. 4). In such nanocrystals, a well-formed CdTe zincblende region could be seen at the junction. Thus, a branched junction forms when the new material initially grows in the zincblende structure, followed by a reversion to anisotropic wurtzite growth, forming the branches. Zincblende formation is favoured by a high supersaturation of the precursors immediately following injection, with wurtzite growth resuming as concentrations drop.

Our approach to synthesizing nanocrystal heterostructures can not only create solution processible analogues of nanowire heterostructures, but also enables unique functionality through the three-dimensional arrangement of components. Representative heterostructures reported here incorporate either type I or type II interfaces to define the nature of the interactions between components. In the first case, CdSe extensions grown on a CdS nanorod are quantum rods separated by a barrier for electrons and holes (Fig. 5a). The coupling of these rods is tuneable by changing the length of the original rod or of the extensions, or selecting a different material to vary the barrier height. *Ab initio* calculation of the electronic structure of model heterostructures confirms that the lowest energy level is split into 'symmetric' and 'anti-symmetric' combinations. A coupling energy of 27 meV was estimated for a heterostructure with a three-monolayer CdS barrier (three layers each of Cd and S) and this coupling energy drops to 9 meV when the CdS barrier is six monolayers thick. Such tuneable coupling, combined with the long spin coherence times observed in colloidal nanocrystals[24], make these heterostructures intriguing candidates for control of quantum coherence.

Branched tetrapods with CdSe central tetrapods and terminal CdTe branches are interesting for their unusual charge-separating properties. These structures absorb light across the visible spectrum, then separate electrons and holes across their type II interfaces. The sharp reduction in spatial overlap between electrons and holes, apparent in the *ab initio* result, effectively quenches the bandgap photoluminescence (Fig. 5b). Both CdSe rods and CdTe tetrapods emit well-defined bandgap luminescence under similar conditions. Calculations have furthermore suggested that electrons localize in the zincblende core of CdSe tetrapods[25]. In the heterostructured branched tetrapods (Fig. 2d), this implies long-range charge separation with the electron at the CdSe zincblende core and the hole delocalized in the outer CdTe branches, 30 nm or more away. This distance can be tuned by the changing dimensions of the central tetrapod. Organic dendrimers designed for such radial charge separation[26] required three generations of growth and purification to separate charges by only a few nanometres. The nature and lifetime of this proposed charge-separated state is currently under investigation, as are possible applications to photovoltaic energy conversion. □

Methods

As an example of heterostructure synthesis, a typical preparation for CdSe/CdTe branched rods dissolved 104 mg of CdO in 0.81 g of octadecylphosphonic acid (PolyCarbon Industries) and 3.19 g of tri(n-octyl)phosphine (TOP) oxide at 300 °C under air-free conditions. At 280 °C, 15.8 mg of selenium dissolved in 320 mg of TOP was injected and the CdSe nanorods grew for four minutes. Then, at 290 °C, 34 mg of tellurium dissolved in 306 mg of TOP was injected and CdTe branches grew for six minutes before the heat was removed to stop the reaction. The resulting heterostructures were deposited from solution onto carbon-coated copper TEM grids for analysis. Low-resolution TEM images were collected on a Philips Tecnai 12 microscope, while HRTEM employed a Philips CM300FEG/UT and a Philips Tecnai G2 20. EDS spectra and line scans were collected on a Philips CM200FEG STEM with a 0.5-nm spot size. Despite this spot size, the spatial resolution was limited by the drift of the instrument so that it remains unclear how compositionally abrupt the heterojunctions are.

The theoretical calculations were done using the charge patching method[27]. This method calculates the band edge states of a nanosystem with *ab initio* accuracy, but scales linearly to the size of the system. The structures were idealized to incorporate abrupt heterojunctions because the actual composition variation is, at this point, unknown. However, we expect the theoretical results to hold qualitatively for less perfect heterostructures. The surface of a nanosystem is passivated with pseudo-hydrogen atoms, for example, one pseudo-hydrogen atom with nuclear charge $Z = 1.5$ electron for each Cd dangling bond, and $Z = 0.5$ electron for each Se, S, or Te dangling bond. This simple model represents an ideal passivation that captures the essence of any good experimental passivations. The atomic positions of a given passivated binary semiconductor nanosystem (that is, CdSe/CdTe, CdSe/CdS) are relaxed using the valence force field (VFF) method. This atomistic method describes the elastic aspects of the system accurately. After the atomic positions of a given system are determined, small prototype systems are precalculated under the local density approximation (LDA) of the density functional theory. The charge densities of these small prototype systems are used to generate localized charge motifs around each atom. The charge motifs for bulk Cd, Se, Te and S atoms and surface pseudo-hydrogen atoms, and the derivatives of these charge motifs regarding the change of bond lengths and bond angles are all generated. These charge motifs and their derivatives are then placed together to generate the LDA charge density of a given nanosystem. The details of this method are reported in ref. 27. The typical error of the so generated charge density compared to the directly calculated charge density under LDA is about 1%. The resulting eigenstate error is about 20–40 meV. The energy splittings between states within the conduction or valence band have typical errors of a few meV. After the charge density is obtained, LDA formulae are used to calculate the LDA total potential and the LDA hamiltonian. Then the folded spectrum method[28,29] is used to calculate the band edge states. Under this procedure, the *ab initio* accuracy band edge states of a thousand-atom nanosystem can be calculated within a few hours on a parallel computer. To calculate coupling energies, a small external electrical field was applied to cancel the permanent dipole of the nanorod[30]. The diameter of the calculated rod shown in Fig. 5a is about 2 nm, the total length is about 9.5 nm, and there are in total 2,002 atoms. For the calculated tetrapod in Fig. 5b, each branch has a diameter of 2.2 nm and a length of 4.2 nm. There are in total 3,685 atoms in the tetrapod.

1. Huynh, W. U., Dittmer, J. J. & Alivisatos, A. P. Hybrid nanorod-polymer solar cells. *Science* **295,** 2425–2427 (2002).
2. Kazes, M., Lewis, D. Y., Ebenstein, Y., Mokari, T. & Banin, U. Lasing from semiconductor quantum rods in a cylindrical microcavity. *Adv. Mater.* **14,** 317–321 (2002).
3. Bruchez, M., Moronne, M., Gin, P., Weiss, S. & Alivisatos, A. P. Semiconductor nanocrystals as fluorescent biological labels. *Science* **281,** 2013–2016 (1998).
4. Schedelbeck, G., Wegscheider, W., Bichler, M. & Abstreiter, G. Coupled quantum dots fabricated by cleaved edge overgrowth: From artificial atoms to molecules. *Science* **278,** 1792–1795 (1997).
5. Bayer, M. *et al.* Coupling and entangling of quantum states in quantum dot molecules. *Science* **291,** 451–453 (2001).
6. Gudiksen, M. S., Lauhon, L. J., Wang, J., Smith, D. C. & Lieber, C. M. Growth of nanowire superlattice structures for nanoscale photonics and electronics. *Nature* **415,** 617–620 (2002).
7. Thelander, C. *et al.* Single-electron transistors in heterostructure nanowires. *Appl. Phys. Lett.* **83,** 2052–2054 (2003).
8. Collier, C. P., Vossmeyer, T. & Heath, J. R. Nanocrystal superlattices. *Annu. Rev. Phys. Chem.* **49,** 371–404 (1998).
9. Ouyang, M. & Awschalom, D. D. Coherent spin transfer between molecularly bridged quantum dots. *Science* **301,** 1074–1078 (2003).
10. Hines, M. A. & Guyot-Sionnest, P. Synthesis and characterization of strongly luminescing ZnS-capped CdSe nanocrystals. *J. Phys. Chem.* **100,** 468–471 (1996).
11. Dabbousi, B. O. *et al.* (CdSe)ZnS core–shell quantum dots: Synthesis and characterization of a size series of highly luminescent nanocrystallites. *J. Phys. Chem. B* **101,** 9462–9475 (1997).
12. Peng, X., Schlamp, M. C., Kadavanich, A. V. & Alivisatos, A. P. Epitaxial growth of highly luminescent CdSe/CdS core/shell nanocrystals with photostability and electronic accessibility. *J. Am. Chem. Soc.* **199,** 7019–7029 (1997).
13. Cao, Y. & Banin, U. Growth and properties of semiconductor core/shell nanocrystals with InAs cores. *J. Am. Chem. Soc.* **122,** 9692–9702 (2000).
14. Kim, S., Fisher, B., Eisler, H.-J. & Bawendi, M. Type II quantum dots: CdTe/CdSe(core/shell) and CdSe/ZnTe(core/shell) heterostructures. *J. Am. Chem. Soc.* **125,** 11466–11467 (2003).
15. Eychmüller, A., Mews, A. & Weller, H. A quantum dot quantum well: CdS/HgS/CdS. *Chem. Phys. Lett.* **208,** 59–62 (1993).
16. Borchert, H. *et al.* Photoemission study of onion like quantum dot quantum well and double quantum well nanocrystals of CdS and HgS. *J. Phys. Chem. B* **107,** 7486–7491 (2003).
17. Manna, L., Scher, E. C. & Alivisatos, A. P. Synthesis of soluble and processable rod-, arrow-, teardrop-, and tetrapod-shaped CdSe nanocrystals. *J. Am. Chem. Soc.* **122,** 12700–12706 (2000).
18. Peng, Z. A. & Peng, X. Nearly monodisperse and shape-controlled CdSe nanocrystals via alternative routes: Nucleation and growth. *J. Am. Chem. Soc.* **124,** 3343–3353 (2002).
19. Manna, L., Milliron, D. J., Meisel, A., Scher, E. C. & Alivisatos, A. P. Controlled growth of tetrapod-branched inorganic nanocrystals. *Nature Mater.* **2,** 382–385 (2003).

20. Yeh, C. Y., Lu, Z. W., Froyen, S. & Zunger, A. Zincblende–wurtzite polytypism in semiconductors. *Phys. Rev. B* **46**, 10086–10097 (1992).

21. Peng, X. *et al.* Shape control of CdSe nanocrystals. *Nature* **404**, 59–61 (2000).

22. Manna, L., Scher, E. C., Li, L. S. & Alivisatos, A. P. Epitaxial growth and photochemical annealing of graded CdS/ZnS shells on colloidal CdSe nanorods. *J. Am. Chem. Soc.* **124**, 7136–7145 (2002).

23. Mokari, T. & Banin, U. Synthesis and properties of CdSe/ZnS core/shell nanorods. *Chem. Mater.* **15**, 3955–3960 (2003).

24. Gupta, J. A., Awschalom, D. D., Peng, X. & Alivisatos, A. P. Spin coherence in semiconductor quantum dots. *Phys. Rev. B* **59**, 10421–10424 (1999).

25. Li, J. & Wang, L. W. Shape effects of electronic states of nanocrystals. *Nano Lett.* **3**, 1357–1363 (2003).

26. Capistosti, G. J., Cramer, S. J., Rajesh, C. S. & Modarelli, D. A. Photoinduced electron transfer within porphyrin-containing poly(amide) dendrimers. *Org. Lett.* **3**, 1645–1648 (2001).

27. Wang, L. W. Charge-density patching method for unconventional semiconductor binary systems. *Phys. Rev. Lett.* **88**, 256402 (2002).

28. Wang, L. W. & Zunger, A. Solving Schrödinger's equation around a desired energy: Application to silicon quantum dots. *J. Chem. Phys.* **100**, 2394–2397 (1994).

29. Canning, A., Wang, L. W., Williamson, A. & Zunger, A. Parallel empirical pseudopotential electronic structure calculations for million atom systems. *J. Comp. Phys.* **160**, 29–41 (2000).

30. Li, L. S. & Alivisatos, A. P. Origin and scaling of the permanent dipole moment in CdSe nanorods. *Phys. Rev. Lett.* **90**, 097402 (2003).

....

Export of dissolved organic carbon from peatlands under elevated carbon dioxide levels

C. Freeman[1], **N. Fenner**[1], **N. J. Ostle**[2], **H. Kang**[1]*, **D. J. Dowrick**[1], **B. Reynolds**[3], **M. A. Lock**[1], **D. Sleep**[2], **S. Hughes**[3] & **J. Hudson**[4]

[1]*School of Biological Sciences, University of Wales, Bangor LL57 2UW, UK*
[2]*Centre for Ecology and Hydrology, Lancaster Environment Centre, Lancaster LA1 4AP, UK*
[3]*Centre for Ecology and Hydrology, Bangor LL57 2UP, UK*
[4]*Centre for Ecology and Hydrology, Wallingford OX10 8BB, UK*

* Present address: Department of Environmental Science and Engineering, Ewha University, Seoul 120-750, Korea

....

Peatlands represent a vast store of global carbon[1]. Observations of rapidly rising dissolved organic carbon concentrations in rivers draining peatlands have created concerns that those stores are beginning to destabilize[2,3]. Three main factors have been put forward as potential causal mechanisms, but it appears that two alternatives—warming[2,4] and increased river discharge[3]—cannot offer satisfactory explanations[5]. Here we show that the third proposed mechanism, namely shifting trends in the proportion of annual rainfall arriving in summer[6], is similarly unable to account for the trend. Instead we infer that a previously unrecognized mechanism—carbon dioxide mediated stimulation of primary productivity—is responsible. Under elevated carbon dioxide levels, the proportion of dissolved organic carbon derived from recently assimilated carbon dioxide was ten times higher than that of the control cases. Concentrations of dissolved organic carbon appear far more sensitive to environmental drivers that affect net primary productivity than those affecting decomposition alone.

Peat-accumulating wetlands have long been recognized as unbalanced ecosystems where the rate of photosynthetic production of organic matter exceeds that of its decomposition[1]. These wetlands have accumulated a vast pool of organic carbon, and currently hold about 390–455 Pg ($1\,Pg = 10^{15}\,g$) of terrestrial C or approaching one-third of the global soil carbon stock[1,7]. Concerns have been expressed that these stores may destabilize, releasing their carbon in either gaseous[1,8] or aqueous form[2,5]. Those concerns appear to be supported by observations of rapidly rising dissolved organic carbon (DOC) concentrations in aquatic ecosystems draining peatland catchments[2]. The trend appears to have been in place for at least 39 years (ref. 5), and is not confined to Europe. In North America, for example, DOC concentrations in streams flowing into a series of boreal lakes were found to increase by 30–80% during one 20-year study[9].

The causes of the observed rises in riverine DOC concentrations are attracting considerable debate[3,5,6]. Some have suggested that the trend is due to increased decomposition in response to rising temperatures[2,5]. Yet field and laboratory studies indicate that DOC concentrations are not sufficiently responsive to warming[2,4] to account for a 65% increase in DOC when temperatures have risen by far less than 1 °C. Experimental manipulations suggest that more than 10 °C of additional warming would be required to yield such a large rise in DOC[2,4]—a level of change not anticipated by even the most pessimistic of IPCC scenarios. Moreover, long-term (21-year) field studies in Canada have failed to find positive correlations between DOC and temperature[10]. Discharge, another alternative[3], seems equally unable to offer a universal explanation. Whereas some studies note that DOC export increases in association with rising discharge[11], other workers have found clear evidence of long-term rises in DOC concentrations without any indication of a trend in discharge[5,6]. A modified hydrological explanation has since been proposed: this suggests that rather than discharge changes alone, it
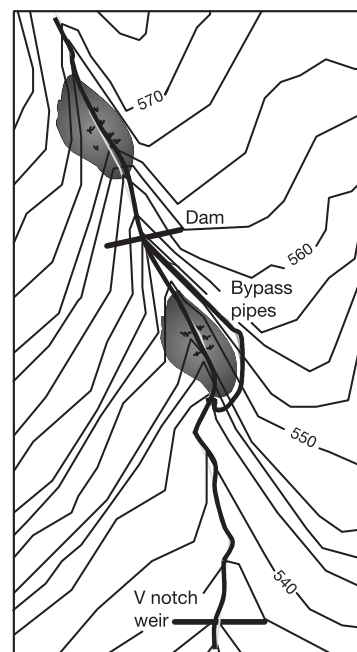

Figure 1 The field-based drought simulation. The hydrological effects of a reduction of summer rainfall were simulated by diverting waterflow around the lower of two wetlands (both wetlands shown shaded). The upper wetland was retained as a control. Contours shown as metres above sea level. The areas of the control and experimental wetlands were 348 m^2 and 336 m^2, respectively.